ISTFA™ 2022: Conference Proceedings from the 48th International
Symposium for Testing and Failure Analysis
October 30–November 3, 2022
Pasadena Convention Center, Pasedena, California, USA
https://doi.org/10.31399/asm.cp.istfa2022p0251

High-Resolution Conductivity Mapping with STEM EBIC

William A Hubbard
NanoElectronic Imaging, Inc., Los Angeles, CA, USA
bhubbard@nanoelectronicimaging.com

Ho Leung Chan, B. C. Regan
University of California Los Angeles, Los Angeles, CA, USA

Abstract

Modern electronic systems rely on components with nanometer-scale feature sizes in which failure can be initiated by atomic-scale electronic defects. These defects can precipitate dramatic structural changes at much larger length scales, entirely obscuring the origin of such an event. The transmission electron microscope (TEM) is among the few imaging systems for which atomic-resolution imaging is easily accessible, making it a workhorse tool for performing failure analysis on nanoscale systems. When equipped with spectroscopic attachments TEM excels at determining a sample's structure and composition, but the physical manifestation of defects can often be extremely subtle compared to their effect on electronic structure. Scanning TEM electron beam-induced current (STEM EBIC) imaging generates contrast directly related to electronic structure as a complement the physical information provided by standard TEM techniques. Recent STEM EBIC advances have enabled access to a variety of new types of electronic and thermal contrast at high resolution, including conductivity mapping. Here we discuss the STEM EBIC conductivity contrast mechanism and demonstrate its ability to map electronic transport in both failed and pristine devices.

Introduction

The TEM is ubiquitous in the study microelectronics, from quality assurance during fabrication to post-failure analysis. Relying on the scattering of electrons which pass through a sample, TEM contrast primarily provides information about the type and arrangement of atoms. Spectroscopic techniques, such as energy dispersive x-ray spectroscopy (EDS) and electron energy loss spectroscopy (EELS), can be deployed in the TEM to more precisely determine sample composition. While these techniques provide valuable structural information, they rarely provide contrast related to the electronic and thermal signals that are often of primary interest when studying function and failure in electronic devices. For example, these standard techniques could locate and identify virtually all atoms in a nanoscale conducting wire but may give no indication of current passing through the wire or the resulting Joule heating until the formation of physical defects (*e.g.* electromigration).

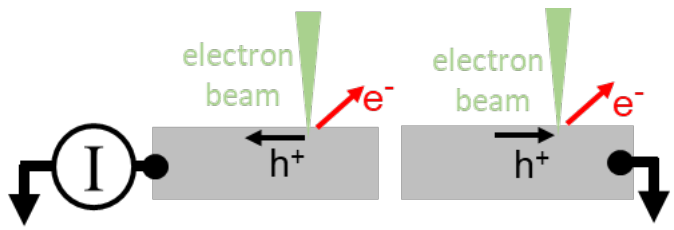

Figure 1: The diagram shows the SEEBIC mechanism on a conductor with a gap in it, similar to the device in Fig. 2. The current meter symbol indicates an EBIC amplifier, here connected to the left side of the conductor; the right side is grounded. SEs, indicated by the red arrows, are emitted by the beam across the entire sample leaving behind holes, indicated in black. Generally, holes produced to the left of the gap will be measured as a positive current (SEEBIC), while the holes to the right of the gap are not measured by the amplifier.

Electron beam-induced current (EBIC) imaging is a decades-old technique for mapping electronic features in an electron microscope. EBIC images are formed by mapping the current generated in a sample, pixel-by-pixel, as it is scanned by an electron beam. Typically performed in the scanning electron microscope (SEM), this technique is occasionally performed in scanning TEM (STEM). The "standard" mode of EBIC, in both SEM and STEM, maps current generated by electric field separation of beam-induced electron-hole pairs, producing images of a sample's local electric fields. More recently [1] a new mode of EBIC was demonstrated in STEM which maps the hole current in a sample resulting from the emission of secondary electrons (SEs), as shown in the Fig. 1 diagram. This secondary electron emission EBIC (SEEBIC) has a much smaller current yield than standard EBIC and has been demonstrated at *much* higher (2 Å) spatial resolution [2]. In SEEBIC, the (unpaired) holes will preferentially reach ground

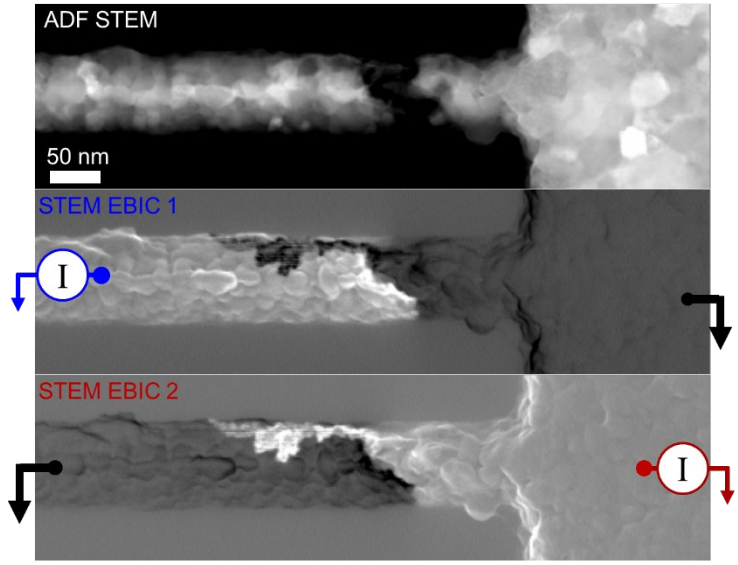

Figure 2: The ADF STEM (upper) image shows an Al wire which has been biased to the point of failure, with a void appearing as the dark gap in the otherwise bright Al wire. STEM EBIC is measured on intact portions of the wire to the left (middle image) and right (lower image) of the void. For each EBIC image, bright (positive) current indicates regions of the wire electrically connected to the EBIC amplifier. Regions inside, and to the left of, the void are, surprisingly, electrically connected to the right side of the broken wire, despite an apparent break in the wire in the ADF STEM image. The pixel size is 1.7 nm, and sharp transitions in the EBIC images occur within a single imaging pixel.

via either the EBIC amplifier, held at virtual ground, or some alternative path to ground directly [3, 4]. The SEEBIC will therefore be stronger in regions where the conductance to the amplifier is greater than alternative paths to ground, producing a resistance contrast image (RCI) [3, 4].

Results and Discussion

The images in Fig. 2 show a simple example of SEEBIC conductivity mapping on a failed metal wire. The 100 nm-wide Al wire is patterned on a thin silicon nitride membrane supported by a Si chip with patterned electrodes [1, 5]. Prior to imaging, current was applied to the wire until Joule heating caused it to fail, producing a void that appears as a dark gap in the wire in the annular dark-field (ADF) STEM image. STEM EBIC is acquired (simultaneously with the ADF image) by connecting the EBIC amplifier to the left side of the wire with the right side grounded (Fig. 2, middle). Another STEM EBIC image is acquired with the EBIC amplifier connected to the right side of the wire and the left grounded (Fig. 2, lower). In both cases positive SEEBIC current (bright signal) is measured on the side of the wire connected to the EBIC amplifier (no standard EBIC is measured as there are no local electric fields). The conductive boundary of the left side of the wire mostly follows the edge of the void as expected from the ADF image. On the right side of the wire, however, the signal is bright in the gap itself, and even in a small region (upper edge of the wire) protruding to the left of the gap. This protrusion may be due to electromigration of material from the gap towards the left, perhaps with the native oxide on the Al surface isolating it from the intact left side of the wire. The nontrivial conductive landscape of the failed wire is not discernable in the ADF STEM image, but is revealed with high contrast in the STEM EBIC image.

The simple example in Fig. 2 gives a roughly binary indication of conductivity (*i.e.* whether or not a region is connected to the EBIC amplifier). For a device connected to both virtual ground (via the EBIC amplifier) and "true" ground, a SEEBIC-derived RCI generally has contrast proportional to the resistance to true ground at each pixel [3, 4]. The broken wire has a sharp, high resistance boundary in the conductive metal wire. Because resistance in the intact portions of the wire is small compared to that of the break, the resistance contrast (SEEBIC signal) does not have a gradient within either side of the wire. (Fig. 2 should not be taken as a rigorous map of resistance, as edge effects increase SEEBIC in some regions; to make a true RCI the signal must be normalized to the total SEEBIC, as discussed in reference [3].)

With the resistance less spatially localized, a SEEBIC RCI map will show a resistance gradient. In Fig. 3, a highly resistive (few GΩ), amorphous strip of GeSbTe (GST) connects two TiN electrodes (also supported by a silicon nitride membrane, similar to the Fig. 2 device). The conductivity of GST increases substantially upon crystallization, a property which makes it the material of choice for phase change memory (PCM). In the Fig. 3 EBIC image, current is measured on the right electrode while the left is held at ground. EBIC from the overlapped TiN/GST region to the left (right) is slightly brighter (darker) than its surroundings due to standard EBIC from the Schottky barrier at the interface. In the non-overlapped regions of TiN and GST there are no local electric fields, and the contrast is due to SEEBIC. Signal is bright on the right TiN electrode, indicating high resistance to the grounded left electrode (low resistance to the EBIC amplifier). The SE yield of GST is larger than that of TiN, but the GST adjacent to the right electrode appears slightly less bright, indicative of to the resistance at the TiN/GST interface. Moving from right to left, the SEEBIC signal (resistance to ground) decreases steadily along the uniformly resistive GST film. The signal on the GST adjacent to the left TiN/GST interface appears slightly brighter than on the TiN electrode alone, again because of the interfacial resistance. The STEM EBIC in Fig. 3 therefore maps the Schottky barriers in the sample, the resulting resistance across the barriers, and the change in resistance to ground moving along the amorphous film, all within a single image.

Conclusions

STEM EBIC provides electronic contrast that is otherwise inaccessible in the TEM, including the ability to visualize electronic transport at high resolution. The SEEBIC conductivity mapping technique demonstrated here can be readily applied to systems with more complex conductivity distributions. Nanoscale next-generation memory architectures present a particularly interesting target, as their function often relies on local conductivity changes upon programming. Applying a sufficient bias to the Fig. 3 GST wire causes heating and crystallization (not shown here) that coincides with an orders-of-magnitude increase in device conductance. STEM EBIC combined with standard TEM techniques can be used to directly correlate crystallographic changes with changes in local conductivity to better understand the switching mechanism. SEEBIC has also been used to image dielectric breakdown in HfO_2-based resistive memory switching [6], visualizing the various stages of breakdown before thermal runaway produces physical damage to the device. In this case, SEEBIC provides a unique opportunity to image the local electronic signatures of a common failure mode *before* failure occurs.

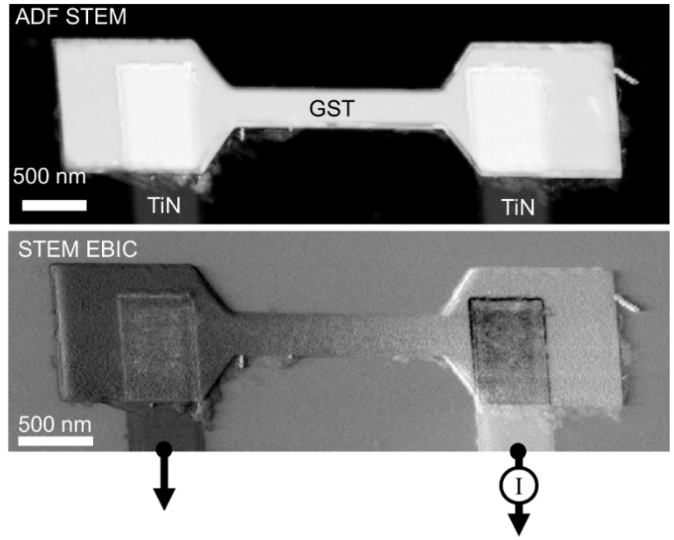

Figure 3: The ADF STEM image shows a strip of GeSbTe (GST) patterned to span two TiN electrodes on a silicon nitride membrane. In the STEM EBIC image, the EBIC amplifier is connected to the right TiN electrode and the left side is connected to ground. The bright and dark rectangles at the left and right overlapping TiN/GST regions, respectively, represent standard EBIC signal from separation of electron-hole pairs in the Schottky barrier at each interface. Outside of the overlapping regions, SEEBIC indicates resistance to the grounded left electrode at each pixel, with a contrast gradient decreasing from right to left.

Acknowledgments

This material is based upon work supported by the Defense Microelectronic Activity under Contract No. HQ072721C0002, and by NSF STC award DMR-1548924 (STROBE), NSF award DMR-2004897, and the Semiconductor Research Corporation (SRC).

References

[1] W. A. Hubbard, *et al.*, “STEM Imaging with Beam-Induced Hole and Secondary Electron Currents,” *Phys. Rev. Applied*, vol. 10, no. 4 (2018), p. 044066. doi: 10.1103/PhysRevApplied.10.044066.

[2] M. Mecklenburg, *et al*., “Electron beam-induced current imaging with two-angstrom resolution,” *Ultramicroscopy*, vol. 207 (2019), p. 112852. doi: 10.1016/j.ultramic.2019.112852.

[3] W. A. Hubbard, *et al.*, “Scanning transmission electron microscope mapping of electronic transport in polycrystalline $BaTiO_3$ ceramic capacitors,” *Appl. Phys. Lett.*, vol. 115, no. 13 (2019), p. 133502. doi: 10.1063/1.5117055.

[4] W. A. Hubbard, *et al*., “STEM EBIC for High-Resolution Electronic Characterization,” in *2020 IEEE International Reliability Physics Symposium (IRPS)*, Dallas, TX, April 2020, pp. 1–5. doi: 10.1109/IRPS45951.2020.9129618.

[5] W. A. Hubbard *et al.*, “Differential electron yield imaging with STXM,” *Ultramicroscopy*, vol. 222 (2021), p. 113198. doi: 10.1016/j.ultramic.2020.113198.

[6] W. A. Hubbard, *et al*., “Imaging Dielectric Breakdown in Valence Change Memory,” *Advanced Functional Materials*, vol. 32, no. 2 (2022), p. 2102313. doi: 10.1002/adfm.202102313.